C. R. Mecanique 346 (2018) 617–633

Contents lists available at ScienceDirect

Comptes Rendus Mecanique

www.sciencedirect.com

Computational modeling of material forming processes / Simulation numérique des procédés de mise en forme

Accounting for local capillary effects in two-phase flows with relaxed surface tension formulation in enriched finite elements

Loïc Chevalier, Julien Bruchon, Nicolas Moulin, Pierre-Jacques Liotier, Sylvain Drapier

Industrial Chair Hexcel – Mines Saint-Étienne, Centre SMS & LGF, UMR CNRS 5307, Mines de Saint-Étienne – Université de Lyon, 158, cours Fauriel, CS 62362, 42023 Saint-Étienne cedex 2, France

ARTICLE INFO

Article history:
Received 26 October 2017
Accepted 9 March 2018
Available online 23 June 2018

Keywords:
Fibrous media
Capillarity
Surface tension
Finite elements
Level-set method

ABSTRACT

This paper introduces a numerical method able to deal with a general bi-fluid model integrating capillary actions. The method relies first on the precise computation of the surface tension force. Considering a mathematical transformation of the surface tension virtual work, the regularity required for the solution on the evolving curved interface is weakened, and the mechanical equilibrium of the triple line can be enforced as a natural condition. Consequently, contact angles of the liquid over the solid phase result naturally from this equilibrium. Second, for an exhaustive representation of capillary actions, pressure jumps across the interface must be accounted for. A pressure enrichment strategy is used to properly compute the discontinuities in both pressure and gradient fields. The resulting method is shown to predict nicely static contact angles for some test cases, and is evaluated on complex 3D cases.

1. Introduction

Capillary-driven flows of matter are involved in a wide range of industrial and natural phenomena [1] [2] [3]. Capillary effects can be depicted as a force per unit length applied at an interface between two phases and originate from the unbalanced forces at the molecular scale on either sides of this interface [4]. Globally [5] [6] [7], three phases can be involved in capillarity: solid, liquid, and vapour phases. Due to the complexity in tracking experimentally capillary effects, a large number of numerical studies have been proposed to investigate industrial cases of capillary flows in porous and fibrous media [8] [9] [10] [11].

The present study focuses on a strategy to compute capillary effects within the context of the simulation of some manufacturing processes for high-performance composites. More especially, Liquid Resin Infusion (LRI) processes are targeted, they consist in the infiltration of a low-viscosity resin into dry fibrous preforms under a low-pressure gradient due to vacuum pulling only (<1 bar) [12] [13]. Some previous works have settled a numerical strategy to model this type of process at the macroscopic scale of the equivalent homogeneous media, *i.e.* where the fibrous preforms are not fully described across the scales [12] [14] [15]. The robustness of this approach has been demonstrated industrially [15], but some recent experi-

E-mail addresses: loic.chevalier@emse.fr (L. Chevalier), bruchon@emse.fr (J. Bruchon), nmoulin@emse.fr (N. Moulin), liotier@emse.fr (P.-J. Liotier), drapier@emse.fr (S. Drapier).

https://doi.org/10.1016/j.crme.2018.06.008
1631-0721/

mental measurements from Pucci et al. [16] have shown that capillary effects may rule the LRI processes to a great extent. Capillary pressures identified in [16] for industrial resin–fibre couples were measured up to 0.3 bar, that is to say one third of the highest pressure differential that can be employed in out-of-autoclave processes such as LRI. Besides, it is known that voids appearing during the infusion process are controlled by the competition between both capillary action and viscous dissipation at the microscopic scale [17]. Accounting for this competition at the scale of the equivalent medium would rely on identified laws and parameters that would hide the complexity of the void creation, migration, and combination [18]. In an attempt to grasp these very local phenomena, the present work aims at setting a robust numerical framework modelling of the capillary effects at the scale of the fibers.

Overall, modelling capillarity faces two main challenges related to the moving and changing liquid–vapour interface: the surface tension combines with the flow front curvature to yield the capillary driving force, and physical discontinuities must be captured across this interface. In the corresponding strongly non-linear problem, the fluid front has to accommodate to verify at the same time the fluid bulk and interfacial equilibria, plus minimise the local surface tension–curvature energy. A linearisation is then mandatory, but still, computing properly the corresponding driving force and discontinuities on the moving curved liquid–vapour interface is a considerable task that can be taken up only by combining stable numerical techniques.

First, regarding the fluid front description, a *level-set* method [19] is used here to follow and capture this interface. It has the advantage to carry a direct representation of the interface. Then, normal vectors and curvatures are explicitly known without any further reconstruction step, unlike the Volume Of Fluid (VOF) technique [20] for instance. Also, this method takes into account topological changes naturally; this is a crucial feature for the study of voids merge and split. When computing the surface tension driving force, a mathematical transformation weakens the regularity required on the interface, since the curvature no longer appears in the problem. Furthermore, the mechanical equilibrium at the junction between solid, liquid, and vapour phases, is subsequently enforced as a natural condition [21], without explicitly considering the contact angle of the liquid over the solid phase. Not prescribing the contact angle is a first step toward a dynamic contact angle representation and permits to rely only on intrinsic properties of the three phases.

The second numerical difficulty comes from the discontinuity of the stress tensor across the fluid–vapour interface. Since viscosities of both liquid and vapour are different, the normal derivatives of the velocity are also discontinuous across the interface [22], and so is the pressure according to the fluid momentum balance. Also, for the same reason, the density contrast between both fluids will induce a pressure gradient jump. Both jumps have to be properly computed since, as shown in the literature [23], errors in the pressure field lead to spurious velocities and then to a degradation of the interface [24] [25]. Various techniques have been proposed in the literature to account for these jumps [26] [27] [28]. Following [29] and Coppola-Owen et al. [30], E-FEM are used here, which consists in enlarging the space of solution for the pressure but with no change in the size of the algebraic system to be solved.

The last technical issue in capillary modelling is the coupling between the flow front motion and the flow mechanical equilibrium, *i.e.* the *level-set* problem and the Stokes equation for the fluid. A fully decoupled staggered strategy is proposed for this.

The paper is organised as follows. In Section 2, the mathematical formulation is introduced for the Stokes equations and the corresponding boundary conditions. Section 3 is devoted to the associated weak formulation that is discretised in space and time in Section 4. Section 5 sets the *level-set* method and the reparametrisation technique used. The staggered coupling approach is described in Section 6. Finally, some simulations of capillary rise of liquid compared with analytic and semi-analytic solutions are presented in Section 7. Based on the observed numerical results some conclusions are finally drawn in Section 8.

2. Mathematical formulation

Let $\Omega \subset \mathbb{R}^3$ be a bounded domain subdivided into two sub-regions denoted $\Omega_{\mathrm{L}}(t)$ for the liquid and $\Omega_{\mathrm{V}}(t)$ for the vapour phase with $\Omega = \Omega_{\mathrm{V}}(t) \cup \Omega_{\mathrm{L}}(t)$, as shown in Fig. 1. The interface between these two fluids is denoted $\Gamma_{\mathrm{LV}}(t) = \partial\Omega_{\mathrm{V}}(t) \cap \partial\Omega_{\mathrm{L}}(t)$, also depending on time. Through the paper, the case of a liquid meniscus forming against a rigid wall, as depicted in Fig. 1, will be used as a baseline for illustrating the method and concepts. In this configuration, the rigid wall (*Solid*) is defined as a boundary of the computational domain. This boundary can be subdivided into two interfaces $\Gamma_{\mathrm{SL}} = \Omega_{\mathrm{L}} \cap \mathit{Solid}$ and $\Gamma_{\mathrm{SV}} = \Omega_{\mathrm{V}} \cap \mathit{Solid}$. Each of the three interfaces Γ_i, for $i \in \{\mathrm{SL}, \mathrm{SV}, \mathrm{LV}\}$, has a normal $\boldsymbol{n}_i$ and two tangents $\boldsymbol{t}_i^1$ and $\boldsymbol{t}_i^2$, along with one in-going tangent $\boldsymbol{T}_i$ normal to its contour (see Fig. 1). Finally, the line at the junction between the three phases (liquid, solid, vapour) is called the triple line and is denoted $L(t) = \Gamma_{\mathrm{SL}} \cap \Gamma_{\mathrm{SV}} \cap \Gamma_{\mathrm{LV}}$.

2.1. Governing equations

In the present work, every fluid is considered as Newtonian, and the corresponding stress tensor is then given by

$$\boldsymbol{\sigma} = -p\boldsymbol{I} + 2\mu\dot{\boldsymbol{\epsilon}}(\boldsymbol{v}), \quad \text{with} \quad \dot{\boldsymbol{\epsilon}}(\boldsymbol{v}) = \frac{1}{2}\left(\nabla\boldsymbol{v} + \nabla\boldsymbol{v}^{\mathsf{T}}\right) \tag{1}$$

with $\boldsymbol{v}$ the velocity, p the pressure and μ the constant viscosity of the fluid (*i.e.* $\mu = \mu_L$, $\forall \boldsymbol{x} \in \Omega_{\mathrm{L}}$ and $\mu = \mu_V$, $\forall \boldsymbol{x} \in \Omega_{\mathrm{V}}$). Assuming that the fluids are incompressible, both momentum balance and mass conservation equations yield the Stokes equations:

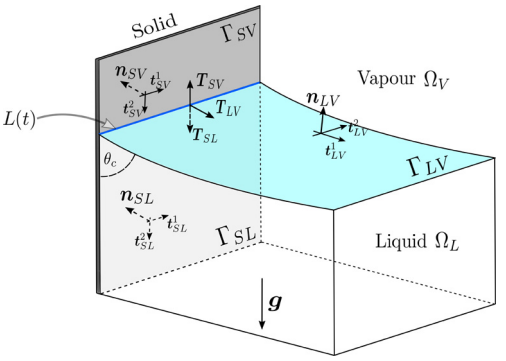

Fig. 1. Schematic of the capillary system – a liquid meniscus against a rigid wall.

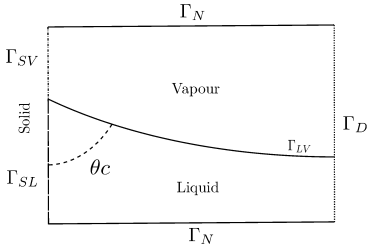

Fig. 2. Boundary condition for a meniscus facing a vertical wall in 2D.

$$\begin{aligned} &\nabla \cdot \boldsymbol{\sigma} + \rho\, \boldsymbol{g} = 0 \\ &\nabla \cdot \boldsymbol{v} = 0 \end{aligned} \tag{2}$$

with $\boldsymbol{g}$ the gravity and ρ the fluid density, which depends on the position in the domain ($\rho = \rho_L$, $\forall \boldsymbol{x} \in \Omega_L$ and $\rho = \rho_V$, $\forall \boldsymbol{x} \in \Omega_V$). At the interface Γ_{LV} between both fluids, the stress vector equilibrium reads

$$-(\boldsymbol{\sigma}_{LV} \cdot \boldsymbol{n}_{LV} + \boldsymbol{\sigma}_{L} \cdot \boldsymbol{n}_{L})_{\Gamma_{LV}} = [\boldsymbol{\sigma} \cdot \boldsymbol{n}]_{\Gamma_{LV}} = -\nabla_\alpha(\gamma_{LV} \boldsymbol{t}^\alpha_{LV}) \tag{3}$$

where classically the jump is denoted $[\cdot]_{\Gamma_{LV}}$ and $\boldsymbol{n} = \boldsymbol{n}_L = -\boldsymbol{n}_{LV}$ is the outgoing normal to the fluid surface. ∇_α is the derivative with respect to the surface coordinate α with an implicit sum on $\alpha = \{1, 2\}$ representing the two tangents. In two dimensions, the surface gradient is reduced to the derivative of the curvilinear abscissa. γ_{LV} is the surface tension between the liquid and vapour phases. Developing Eq. (3) yields the more usual expression

$$[\boldsymbol{\sigma} \cdot \boldsymbol{n}]_{\Gamma_{LV}} = -\gamma_{LV} \mathcal{C} \boldsymbol{n} - (\nabla_\alpha \gamma_{LV}) \boldsymbol{t}^\alpha_{LV} \tag{4}$$

where the first term expresses the Laplace's law, with $\mathcal{C}$ the curvature, while the second term, accounting for surface tension gradients, is the Marangoni term. This study is based on Eq. (3), taking into account both Laplace's law and Marangoni's effect, and making it possible, as it will be seen, to enforce naturally the mechanical equilibrium at the triple junction.

2.2. Boundary conditions

The boundary of the domain Ω is split into three zones depending on the boundary conditions applied, namely Neumann, Dirichlet, and boundary conditions applied on the rigid wall: $\partial\Omega = \Gamma_N \cup \Gamma_D \cup \Gamma_{SL} \cup \Gamma_{SV}$, as illustrated in Fig. 2 for the specific case of a meniscus in 2D.

- The classical Dirichlet and Neumann boundary conditions for our case are $\boldsymbol{v} = \bar{\boldsymbol{v}}$ on Γ_D and $\boldsymbol{\sigma} \cdot \boldsymbol{n} = -P_{ext} \boldsymbol{n}$ on Γ_N, respectively. Notice that, for the sake of simplicity, all the velocity components are assumed to be imposed in this section. However, in the "Numerical experiments" section, the Dirichlet condition will be applied either to all the velocity components, or only to the tangential or normal components, depending on the location on the boundary Γ_D.
- On the solid wall, the surface tension generates a tangent velocity, which may induce friction and can be cast as:

$$\begin{aligned} &\boldsymbol{v} \cdot \boldsymbol{n}_{SL} = 0 \quad \text{and} \quad \boldsymbol{\sigma} \cdot \boldsymbol{n}_{SL} = -\beta_{SL} \boldsymbol{v} + \nabla_\alpha(\gamma_{SL} \boldsymbol{t}^\alpha_{SL}) \qquad \text{on } \Gamma_{SL} \\ &\boldsymbol{v} \cdot \boldsymbol{n}_{SV} = 0 \quad \text{and} \quad \boldsymbol{\sigma} \cdot \boldsymbol{n}_{SV} = -\beta_{SV} \boldsymbol{v} + \nabla_\alpha(\gamma_{SV} \boldsymbol{t}^\alpha_{SV}) \qquad \text{on } \Gamma_{SV} \end{aligned} \tag{5}$$

  because one part of the wall is in contact with the liquid and the other part is in contact with the vapour. The coefficient β is a friction coefficient depending on the surrounding fluid ($\beta = \beta_{SL}$, $\forall \boldsymbol{x} \in \Gamma_{SL}$ and $\beta = \beta_{SV}$, $\forall \boldsymbol{x} \in \Gamma_{SV}$) aiming at

accounting for the dynamic sub-scale effects [31]. Choosing $\beta = 0$ leads to a free slip condition, governed only by the capillary effects on the wall. Introducing this friction changes the dynamic, but has no effect on the steady-state solution that is targeted here.

At the triple line $L(t)$, which is the intersection between the three phases (solid, liquid, vapour) such as depicted in Fig. 1, the mechanical equilibrium reads

$$\gamma_{SL}\boldsymbol{T}_{SL} + \gamma_{SV}\boldsymbol{T}_{SV} + \gamma_{LV}\boldsymbol{T}_{LV} = \boldsymbol{R}_{solid} \tag{6}$$

It is assumed that the reaction of the solid $\boldsymbol{R}_{solid}$ has no tangent component ($\boldsymbol{R}_{solid} = R_{solid}\boldsymbol{n}_s$, with $\boldsymbol{n}_s$ the normal to the solid which is equal to $\boldsymbol{n}_{SL}$ or $\boldsymbol{n}_{SV}$ at the triple line – see Fig. 1). The fluid normal velocity vanishes because the solid is rigid, $\boldsymbol{v}\cdot\boldsymbol{n}_s = 0$. This approximation is in good accordance with an article by Sauer [32], where the solid reaction is cancelled considering the scale of observation chosen in this study. Therefore, only the projection of Eq. (6) in the tangent direction of the solid is used.

Finally, the final problem of two immiscible fluids against a rigid wall (see Fig. 1, also) can be expressed as follows:

$$\begin{aligned}
&\mu\Delta\boldsymbol{v} - \nabla p = -\rho\boldsymbol{g} && \text{in } \Omega\\
&\nabla\cdot\boldsymbol{v} = 0 && \text{in } \Omega\\
&\boldsymbol{\sigma}\cdot\boldsymbol{n} = -P_{ext}\boldsymbol{n} && \text{on } \Gamma_N\\
&[\boldsymbol{\sigma}\cdot\boldsymbol{n}]_{\Gamma_{LV}} = -\nabla_\alpha(\gamma_{LV}\boldsymbol{t}^\alpha_{LV}) && \text{on } \Gamma_{LV}(t)\\
&\boldsymbol{v}\cdot\boldsymbol{n}_{SL} = 0 \quad\text{and}\quad \boldsymbol{\sigma}\cdot\boldsymbol{n}_{SL} = -\beta_{SL}\boldsymbol{v} + \nabla_\alpha(\gamma_{SL}\boldsymbol{t}^\alpha_{SL}) && \text{on } \Gamma_{SL}(t)\\
&\boldsymbol{v}\cdot\boldsymbol{n}_{SV} = 0 \quad\text{and}\quad \boldsymbol{\sigma}\cdot\boldsymbol{n}_{SV} = -\beta_{SV}\boldsymbol{v} + \nabla_\alpha(\gamma_{SV}\boldsymbol{t}^\alpha_{SV}) && \text{on } \Gamma_{SV}(t)\\
&\gamma_{SL}\boldsymbol{T}_{SL} + \gamma_{SV}\boldsymbol{T}_{SV} + \gamma_{LV}\boldsymbol{T}_{LV} = R_{solid}\boldsymbol{n}_s \quad\text{and}\quad \boldsymbol{v}\cdot\boldsymbol{n}_s = 0 && \text{on } L(t)\\
&\boldsymbol{v} = \overline{\boldsymbol{v}} && \text{on } \Gamma_D
\end{aligned} \tag{7}$$

3. Weak formulation

In order to solve the previous system of equations (7) using the Finite Element Method (FEM), the weak form of this system has first to be established. Let us introduce the function spaces based on the Lesbesgues $L^2(\Omega)$ and Sobolev $\mathcal{H}^1(\Omega)$ spaces

$$\begin{aligned}
&\mathcal{W} = \{\boldsymbol{\xi}\in(\mathcal{H}^1(\Omega))^3 \mid \boldsymbol{\xi} = \bar{\boldsymbol{v}} \text{ on } \Gamma_D, \boldsymbol{\xi}\cdot\boldsymbol{n} = 0 \text{ on } \Gamma_{SL}\cup\Gamma_{SV}\}\\
&Q = \{\zeta\in L^2(\Omega) \mid \int_\Omega \zeta\,\mathrm{d}V = 0\}
\end{aligned} \tag{8}$$

Following the Galerkin approach, both impermeability of the wall and Dirichlet boundary conditions are included in the definition of the approximation space $\mathcal{W}$ (essential boundary condition). Let the space $\mathcal{W}^0$ be a restriction of $\mathcal{W}$ such that $\mathcal{W}^0 = \{\boldsymbol{\xi}\in(\mathcal{H}^1(\Omega))^3 \mid \boldsymbol{\xi} = \boldsymbol{0} \text{ on } \Gamma_D, \boldsymbol{\xi}\cdot\boldsymbol{n} = 0 \text{ on } \Gamma_{SL}\cup\Gamma_{SV}\}$, from which the velocity test function will be chosen. Weighting the Stokes equations (2) by the test functions, and after integrations by parts, one obtains:

$$-\int_\Omega p\nabla\cdot\boldsymbol{w}\,\mathrm{d}V + \int_\Omega \mu\nabla\boldsymbol{v}:\nabla\boldsymbol{w}\,\mathrm{d}V - \int_\Omega q\nabla\cdot\boldsymbol{v}\,\mathrm{d}V = \int_\Omega \rho\boldsymbol{g}\cdot\boldsymbol{w}\,\mathrm{d}V + \underbrace{\int_{\partial\Omega_L\cup\partial\Omega_V} \boldsymbol{\sigma}\cdot\boldsymbol{n}\cdot\boldsymbol{w}\,\mathrm{d}S} \tag{9}$$

for any test function $\boldsymbol{w}\in\mathcal{W}^0$ and $q\in\mathcal{Q}$.

Let us now work out the natural boundary conditions, the last term in the weak formulation (Eq. (2)), to detail the contributions of the remaining conditions. The integral contribution over the domain boundary can be split into three terms, as depicted in Fig. 1: respectively, the liquid boundary $\partial\Omega_L$, the vapour boundary $\partial\Omega_V$, and the liquid–vapour interface Γ_{LV}. On both fluid boundaries, Dirichlet as well as Neumann conditions apply, such as illustrated in Fig. 2 for a 2D case. Then, considering that the test functions $\boldsymbol{w}$ vanish over Γ_D, the initial integral on the boundaries turns into integrals on the three interfaces Γ_i, with $i\in\{SL, SV, LV\}$ plus the boundary where Neumann conditions prevail.

$$\begin{aligned}
&\int_{\partial\Omega_L\cup\partial\Omega_V} \boldsymbol{\sigma}\cdot\boldsymbol{n}\cdot\boldsymbol{w}\,\mathrm{d}S\\
&= \int_{\partial\Omega_L\setminus\Gamma_{LV}} \boldsymbol{\sigma}\cdot\boldsymbol{n}\cdot\boldsymbol{w}\,\mathrm{d}S + \int_{\partial\Omega_V\setminus\Gamma_{LV}} \boldsymbol{\sigma}\cdot\boldsymbol{n}\cdot\boldsymbol{w}\,\mathrm{d}S - \int_{\Gamma_{LV}} (\boldsymbol{\sigma_{LV}} - \boldsymbol{\sigma_L})\cdot\boldsymbol{n}\cdot\boldsymbol{w}\,\mathrm{d}S - \int_{\Gamma_N} P_{ext}\boldsymbol{n}\cdot\boldsymbol{w}\,\mathrm{d}S
\end{aligned} \tag{10}$$

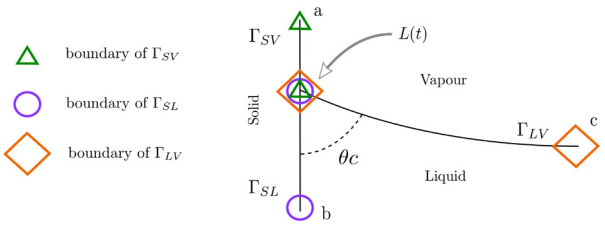

Fig. 3. Meniscus facing a wall in 2D with boundary of each interface.

Consequently, the boundary condition corresponding to a potential friction over the wall on Γ_{SL} and Γ_{SV} (Eq. (5)), and the jump of normal stress across the interface Γ_{LV} (Eq. (3) are weakly imposed. This crucial contribution finally reads

$$\begin{aligned}&\int_{\partial\Omega_L\cup\partial\Omega_V} \boldsymbol{\sigma}\cdot\boldsymbol{n}\cdot\boldsymbol{w}\,\mathrm{d}S\\ &=\int_{\Gamma_{SL}}\left(-\beta_{SL}\boldsymbol{v}+\nabla_\alpha(\gamma_{SL}\boldsymbol{t}^\alpha)\right)\cdot\boldsymbol{w}\,\mathrm{d}S+\int_{\Gamma_{SV}}\left(-\beta_{SV}\boldsymbol{v}+\nabla_\alpha(\gamma_{SV}\boldsymbol{t}^\alpha)\right)\cdot\boldsymbol{w}\,\mathrm{d}S+\int_{\Gamma_{LV}}\nabla_\alpha(\gamma_{LV}\boldsymbol{t}^\alpha)\cdot\boldsymbol{w}\,\mathrm{d}S\\ &-\int_{\Gamma_N}P_{ext}\boldsymbol{n}\cdot\boldsymbol{w}\,\mathrm{d}S\end{aligned}\tag{11}$$

It is classical in the literature to perform an integration by parts on the term $\nabla_\alpha(\gamma\boldsymbol{t}^\alpha)$ [33] [34] in order to ease the computation, because the derivative is reported on the test function. Surface tension and surface energy terms are transformed into

$$\int_{\Gamma_i}\nabla_\alpha(\gamma_i\boldsymbol{t}_i^\alpha)\cdot\boldsymbol{w}\,\mathrm{d}S=\int_{\partial\Gamma_i}\gamma_i\boldsymbol{T}_i\cdot\boldsymbol{w}\,\mathrm{d}l-\int_{\Gamma_i}\gamma_i(\boldsymbol{I}-\boldsymbol{n}_i\otimes\boldsymbol{n}_i):\nabla\boldsymbol{w}\,\mathrm{d}S,\quad\text{with } i\in\{\mathrm{LV},\mathrm{SL},\mathrm{SV}\}\tag{12}$$

Applying this integration for the three interfaces, as suggested by Bruchon [21], has the advantage to weakly impose the mechanical equilibrium at the triple line, which is the last natural boundary condition. $\partial\Gamma_i$ represents the boundary of the interface Γ_i, with $i\in\{\mathrm{SL},\mathrm{SV},\mathrm{LV}\}$, corresponding to points in 2D, whereas it becomes lines in 3D. Each term $\int_{\partial\Gamma_i}\gamma_i\boldsymbol{T}_i\cdot\boldsymbol{w}\,\mathrm{d}l$ can be split into a contribution on the triple line $L(t)$ and the complementary region $\partial\Gamma_i\setminus L(t)$, as shown in Fig. 3 for a 2D case. Then summing over i the first term in Eq. (12) leads to:

$$\begin{aligned}&\int_{\partial\Gamma_{SV}}\gamma_{SV}\boldsymbol{T}_{SV}\cdot\boldsymbol{w}\,\mathrm{d}l+\int_{\partial\Gamma_{SL}}\gamma_{SL}\boldsymbol{T}_{SL}\cdot\boldsymbol{w}\,\mathrm{d}l+\int_{\partial\Gamma_{LV}}\gamma_{LV}\boldsymbol{T}_{LV}\cdot\boldsymbol{w}\,\mathrm{d}l\\ &=\underbrace{\int_{L(t)}\underbrace{(\gamma_{SV}\boldsymbol{T}_{SV}+\gamma_{SL}\boldsymbol{T}_{SL}+\gamma_{LV}\boldsymbol{T}_{LV})\cdot\boldsymbol{w}}_{=R_{solid}\boldsymbol{n}_s\cdot\boldsymbol{w}}\,\mathrm{d}l}_{=0}+\sum_{i\in\{\mathrm{SL},\mathrm{SV},\mathrm{LV}\}}\int_{\partial\Gamma_i\setminus L(t)}\gamma_i\boldsymbol{T}_i\cdot\boldsymbol{w}\,\mathrm{d}l\end{aligned}\tag{13}$$

The first term of Eq. (13) corresponds to the contribution of each interface at the triple line, whereas the second term is the contribution on the remaining boundary of each interface, typically the positions a, b, and c in Fig. 3 for a 2D case. Due to the restriction on the test function, the boundary tangent term vanishes if a Dirichlet boundary condition is prescribed at these points. In Eq. (13), the surface tensions equilibrium over the triple line is verified because the wall is assumed to be rigid ($\boldsymbol{w}\cdot\boldsymbol{n_S}=0$ on $L(t)$). But for soft solids this term is mandatory, and can even prevail in some circumstances [35].

Finally, the weak form of the Stokes equation for two fluids in contact with a wall is:
find $\boldsymbol{v}\in\mathcal{W}$ and $p\in Q$ such that

$$\begin{aligned}&-\int_\Omega p\nabla\cdot\boldsymbol{w}\,\mathrm{d}V+\int_\Omega\mu\nabla\boldsymbol{v}:\nabla\boldsymbol{w}\,\mathrm{d}V-\int_\Omega q\nabla\cdot\boldsymbol{v}\,\mathrm{d}V+\int_{\Gamma_{solid}}\beta\boldsymbol{v}\cdot\boldsymbol{w}\,\mathrm{d}S\\ &=\int_\Omega\rho\boldsymbol{g}\cdot\boldsymbol{w}\,\mathrm{d}V-\int_\Gamma\gamma(\boldsymbol{I}-\boldsymbol{n}\otimes\boldsymbol{n}):\nabla\boldsymbol{w}\,\mathrm{d}S-\int_{\Gamma_N}P_{ext}\boldsymbol{w}\cdot\boldsymbol{n}\,\mathrm{d}S+\int_{\partial\Gamma\setminus L}\gamma\boldsymbol{T}\cdot\boldsymbol{w}\,\mathrm{d}l\end{aligned}\tag{14}$$

for any test functions $\boldsymbol{w}\in\mathcal{W}^0$ and $q\in\mathcal{Q}$, with

$$\begin{aligned}
&\int_{\Gamma_{\text{solid}}} \beta \boldsymbol{v}\cdot\boldsymbol{w}\,\mathrm{d}S = \sum_{j\in\{\text{SL,SV}\}}\int_{\Gamma_j}\beta_j\boldsymbol{v}\cdot\boldsymbol{w}\,\mathrm{d}S\\
&\int_{\Gamma}\gamma(\boldsymbol{I}-\boldsymbol{n}\otimes\boldsymbol{n}):\nabla\boldsymbol{w}\,\mathrm{d}S = \sum_{i\in\{\text{SL,SV,LV}\}}\int_{\Gamma_i}\gamma_i(\boldsymbol{I}-\boldsymbol{n}_i\otimes\boldsymbol{n}_i):\nabla\boldsymbol{w}\,\mathrm{d}S\\
&\int_{\partial\Gamma\setminus L}\gamma\boldsymbol{T}\cdot\boldsymbol{w}\,\mathrm{d}l = \sum_{i\in\{\text{SL,SV,LV}\}}\int_{\partial\Gamma_i\setminus L(t)}\gamma_i\boldsymbol{T}_i\cdot\boldsymbol{w}\,\mathrm{d}l
\end{aligned} \tag{15}$$

4. Discretisation

In order to establish the finite element formulation, the space and time discretisation of the global problem formulated in Eqs. (14)–(15) is described in this section.

4.1. Space discretisation

Let the computational domain Ω be discretised by a structured or unstructured mesh, $\mathcal{T}_h$, made up of triangles in 2D and tetrahedrons in 3D. Velocity $\boldsymbol{v}$ and pressure p fields are approximated respectively by $\boldsymbol{v}_h$ and p_h, which are both continuous and piecewise linear functions (P1/P1 approximation). Because the piecewise linear approximation for pressure and velocity is not stable for the Stokes problem, a stabilisation technique is required in order to circumvent the Ladyzhenskaya–Babuska–Brezzi (LBB) condition. The stabilisation used here belongs to the Variational Multiscale Method (VMS) framework, formalised by Hughes [36] [37], and is more precisely the Algebraic SubGrid Scale (ASGS) derived by Codina [38]. From the VMS method, both velocity and pressure are decomposed into a computable component, the finite element solution, and a subgrid component. The specificity of the ASGS method is to choose the subgrid component for the velocity related to the finite element residual of the momentum balance equation, whereas the subgrid component of the pressure is related to the finite element residual of the mass balance equation. Hence, on a mesh element e:

$$\begin{aligned}
&\boldsymbol{v}_{|e} \approx \boldsymbol{v}_{h|e} - \tau_q^e\nabla p_{h|e} + \tau_q^e\rho_{|e}\boldsymbol{g}\\
&p_{|e} \approx p_{h|e} - \tau_v^e\nabla\cdot\boldsymbol{v}_{h|e}
\end{aligned} \tag{16}$$

with the coefficients $\tau_v^e = \frac{h_e^2}{\mu}$, $\tau_q^e = \mu$, and h_e the mesh size of element e. An integration by parts is performed on the finite element residual for the velocity, as explained in [38]. This stabilisation is widely used [39] and is a proven method that has been successfully employed for our various processes controlled by fluid flows [40] [2] [41].

Another consequence of the continuous approximation of both pressure and velocity is that classical Galerkin-based FE are intrinsically not able to capture a discontinuous solution. As explained earlier, both the surface tension and the change in density may lead to discontinuities in pressure and pressure gradient, respectively. It is crucial to compute accurately these jumps, otherwise the front of the fluid degenerates, independently of the method used to capture it. Few strategies are proposed in the literature to overcome this issue. It is possible to take advantage of the known pressure discontinuity from the Laplace law, remove the discontinuity, and during a post-processing stage add it back [26]. A different idea is to place additional unknowns on the interface at each time step (X-FEM method) [27] [28], and thus increase the pressure space dimension. Yet, this method increases the size of the system and the connectivity has to be updated during computations. Also, a strategy has to be used to circumvent the problem of the system's ill-conditioning [42]. The last method exposed in the literature consists in adding some degrees of freedom to enrich the approximation space, but condense them prior to solving the algebraic system (E-FEM) [30]. Following Ausas et al. [29], two degrees of freedom are needed to capture the pressure jump. Also, Coppola-Owen et al. [30] proved that one complementary degree of freedom is sufficient for representing the pressure gradient jump that originates from the density contrast between both phases. The asset of the E-FEM used in this paper is that the size of the system remains unchanged since the three added degrees of freedom are condensed prior to assembly.

Furthermore, to compute accurately the contribution of the diffusion and gravity terms in the elements cut by the interface, a special attention has to be paid to adapt the quadrature rules. More precisely, each tetrahedron (triangle in 2D) cut by the interface is virtually divided into six sub-tetrahedrons (three sub-triangles) to which are applied the same integration rule as the non-cut elements [2]. Since one integration point is required to integrate the linear contributions, and considering a viscosity and density constant in each phase, only one integration point is required into each sub-element.

4.2. Time discretisation

The time is sequenced into increments, the superscript $(\cdot)^n$ denotes a quantity at time n, and $\Delta t = t^{n+1} - t^n$ is the time step between two increments. The weak form of the global equilibrium (Eq. (14)) requires to compute the driving force term associated with surface tension at time t^{n+1}

$$\int_{\Gamma^{n+1}} \gamma (\boldsymbol{I} - \boldsymbol{n} \otimes \boldsymbol{n})^{n+1} : \nabla \boldsymbol{w} \, \mathrm{d}s \tag{17}$$

This non-linear problem of a moving interface with a surface tension force acting on it implies the use of small time steps to cope with potential severe non-linearities. A precise approximation of the position of the interface and its normal is required; otherwise, the interface degenerates rapidly. To overcome this difficulty, it is possible to use a semi-implicit time treatment on the surface tension term [43]. The position of the interface at time t^{n+1} is approximated by its position known at time t^n plus the distance travelled during the time increment, $\Delta t \, \boldsymbol{v}^{n+1}$. This prediction of the interface position is then used to compute the surface tension's contribution.

Let id be the identity function $id : \mathbb{R}^3 \to \mathbb{R}^3$ with $id(\boldsymbol{x}) = \boldsymbol{x}$. Then the time discretisation of the surface tension term reads

$$\begin{aligned} \int_{\Gamma^{n+1}} \gamma (\boldsymbol{I} - \boldsymbol{n} \otimes \boldsymbol{n})^{n+1} : \nabla \boldsymbol{w} \, \mathrm{d}s &= \int_{\Gamma^{n+1}} \gamma \nabla_\Gamma \boldsymbol{id}^{n+1} : \nabla \boldsymbol{w} \, \mathrm{d}S \\ &\approx \int_{\Gamma^n} \gamma \nabla_\Gamma (\boldsymbol{id}^n + \Delta t \boldsymbol{v}^{n+1}) : \nabla \boldsymbol{w} \, \mathrm{d}S \\ &= \int_{\Gamma^n} \gamma (\boldsymbol{I} - \boldsymbol{n} \otimes \boldsymbol{n})^n : \nabla \boldsymbol{w} \, \mathrm{d}S + \Delta t \int_{\Gamma^n} \gamma \left(\nabla \boldsymbol{v}^{n+1} (\boldsymbol{I} - \boldsymbol{n} \otimes \boldsymbol{n})^n \right) : \nabla \boldsymbol{w} \, \mathrm{d}S \end{aligned} \tag{18}$$

with ∇_Γ the surface gradient operator. This discretisation was proposed by Bänsch [44], based on previous work by Dziuk and coworkers for the Laplace–Beltrami operator [45] [46]. Groß et al. [47] performed an error analysis and showed a $O(\sqrt{h})$ error bound for this approximation. The second term in the previous equation (18) is a dissipation term that acts as a stabilisation term.

5. *Level-set* method

The *level-set* method introduced by Osher et al. [19] has the advantage to give an implicit representation of the interface between the vapour and the liquid phases. The *level set* is a time-dependent scalar function, $\phi(\boldsymbol{x}, t)$, representing the signed distance to the front of fluid. The implicit representation of the interface is given by $\Gamma_{\mathrm{LV}}(t) = \{\boldsymbol{x} \mid \phi(\boldsymbol{x}, t) = 0\}$. To follow the physics modelled, the *level-set* function is convected using a transport equation, with the considered velocity $\boldsymbol{v}$

$$\frac{\partial \phi}{\partial t} + \boldsymbol{v} \cdot \nabla \phi = 0 \tag{19}$$

In order to solve the above hyperbolic equation, one needs an initial condition $\phi(\boldsymbol{x}, 0)$ and a Dirichlet boundary condition on the inflow boundary $\partial\Omega_{\mathrm{in}} = \{\boldsymbol{x} \in \partial\Omega \mid \boldsymbol{v} \cdot \boldsymbol{n} < 0\}$. The equation is solved with a Finite Element Method using the same grid as for the fluid problem. The level-set function ϕ is consequently approximated by ϕ_h, a continuous and piecewise linear function. As the standard Galerkin approximation is not stable for the hyperbolic equation (19), we use the Streamline Upwind Petrov–Galerkin (SUPG) approach developed by Brooks and Hughes [48]. Then, the discrete test function $\tilde{\phi}_h^*$ is chosen on an element e as

$$\tilde{\phi}_{h|e}^* = \phi_{h|e}^* + \tau^e \boldsymbol{v}_{|e} \cdot \nabla \phi_{h|e}^*$$

where ϕ_h^* is the standard piecewise linear test function, and the stabilisation coefficient is defined as

$$\tau^e = \frac{1}{2} \frac{h_e}{|\boldsymbol{v}_{|e}|}$$

with $|\boldsymbol{v}_{|e}|$ the norm of the average velocity on the element e. The SUPG method creates an 'up-wind' effect by adding diffusion in the direction of the convective velocity. Finally, for the time discretisation, a Crank–Nicolson scheme [49] is used with a quadratic convergence error.

The signed-distance property $\|\nabla \phi\| = 1$ is not conserved by the convection of ϕ with the velocity field $\boldsymbol{v}$. Consequently, sharp gradients may develop at the interface. In that case, the SUPG is not able to stabilise the convective term and the *level set* may get severely distorted. To recover the unitary gradient property, the Hamilton–Jacobi equation is solved [50]

$$\begin{cases} \dfrac{\partial \varphi}{\partial \tau} + \mathrm{sign}(\phi)(\|\nabla \varphi\| - 1) = 0 \\ \varphi(x, \tau = 0) = \phi(x, t) \end{cases} \tag{20}$$

with τ a fictive time and $\mathrm{sign}(\phi)$ a sign function that could be defined from Peng [51] as

$$\operatorname{sign}(\phi) = \frac{\phi}{\sqrt{\phi^2 + ||\nabla\phi||^2 h_e^2}} \tag{21}$$

Introducing the convective velocity $\boldsymbol{v}_r = \operatorname{sign}(\phi)\frac{\nabla\varphi}{||\nabla\varphi||}$ and $F = \operatorname{sign}(\phi)$ makes it possible to get the Hamilton–Jacobi equation (20) back to a transport equation such as Eq. (19) with a right-hand side

$$\frac{\partial\varphi}{\partial\tau} + \boldsymbol{v}_r \cdot \nabla\varphi = F \tag{22}$$

The previous equation should be solved until reaching the steady-state solution. In our simulations, only three pseudo-time steps are enough to control the gradient of the level-set function in the vicinity of the interface. Finally, the non-linearity of the Hamilton–Jacobi equation is removed by considering the velocity $\boldsymbol{v}_r$ at the previous pseudo-time step. Accordingly, this equation can be solved exactly in the same way as the *level-set* transport equation (19).

6. Temporal coupling strategy

The time sequence used in the presented simulations consists in computing successively velocity–pressure fields and then updating the *level-set* function, once and only once in a time step: at a time t^{n+1}, Stokes equations are solved using the geometry evaluated at t^n. The corresponding staggered algorithm is given in Algo. 1. The symbol $\sum_e$ in the Stokes equations stands for the summation over all the mesh elements e, and is involved in the terms resulting from the ASGS stabilisation technique.

Algorithm 1 Staggered algorithm for Stokes and *level-set* problems.

Require: ϕ_h^0 and $\boldsymbol{v}_h^0$, the initial values

for all $t^{n+1} \in]0, T]$ **do**

- **Step 1** find $\boldsymbol{v}_h^{n+1} \in \boldsymbol{\mathcal{V}}_h$ and $p_h^{n+1} \in Q_h$ such that

$$\begin{aligned}
&-\int_{\Omega_h} p_h^{n+1}\nabla\cdot\boldsymbol{w}_h\,\mathrm{d}V + \int_{\Omega_h}\mu^n\nabla\boldsymbol{v}_h^{n+1} : \nabla\boldsymbol{w}_h\,\mathrm{d}V - \int_{\Omega_h} q_h\nabla\cdot\boldsymbol{v}_h^{n+1}\,\mathrm{d}V + \int_{\Gamma_{\mathrm{solid},h}}\beta\boldsymbol{v}_h^{n+1}\cdot\boldsymbol{w}_h\,\mathrm{d}S \\
&\qquad + \sum_e \tau_q^{e,n}\int_e \nabla\cdot\boldsymbol{v}_h^{n+1}\nabla\cdot\boldsymbol{w}_h\,\mathrm{d}V - \sum_e\tau_v^{e,n}\int_e\nabla p_h^{n+1}\nabla q_h\,\mathrm{d}V \\
&\qquad = \int_{\Omega_h}\rho^n\boldsymbol{g}\cdot\boldsymbol{w}_h\,\mathrm{d}V - \int_{\Gamma_h^n}\gamma(\boldsymbol{I}-\boldsymbol{n}\otimes\boldsymbol{n})^n : \nabla\boldsymbol{w}_h\,\mathrm{d}S \\
&-\Delta t\int_{\Gamma_h^n}\gamma\left(\nabla\boldsymbol{v}_h^{n+1}(\boldsymbol{I}-\boldsymbol{n}\otimes\boldsymbol{n})^n\right) : \nabla\boldsymbol{w}_h\,\mathrm{d}S + \int_{\partial\Gamma_h\setminus L}\gamma\boldsymbol{T}\cdot\boldsymbol{w}_h\,\mathrm{d}l - \sum_e\tau_v^{e,n}\int_e\rho\boldsymbol{g}\cdot\nabla q_h\,\mathrm{d}V
\end{aligned}$$

  for any test functions $\boldsymbol{w}_h \in \boldsymbol{\mathcal{V}}_h^0$ and $q_h \in \mathcal{Q}_h$.

- **Step 2** find $\phi_h \in \mathcal{S}_h$ such that

$$\int_{\Omega_h}\frac{\phi_h^{n+1}-\phi_h^n}{\Delta t}\tilde{\phi}_h^*\,\mathrm{d}V + \frac{1}{2}\int_{\Omega_h}\boldsymbol{v}_h^{n+1}\cdot\nabla\phi_h^{n+1}\tilde{\phi}_h^*\,\mathrm{d}V = -\frac{1}{2}\int_{\Omega_h}\boldsymbol{v}_h^n\cdot\nabla\phi_h^n\tilde{\phi}_h^*\,\mathrm{d}V$$

  with $\tilde{\phi}_h^* = \phi_h^* + \tau_k\boldsymbol{v}_h^{n+1}\cdot\nabla\phi_h^*$ for any test functions $\phi_h^* \in \mathcal{S}_h^0$

- **Step 3** Reinitialisation step: solve the Hamilton–Jacobi (22).

end for

7. Numerical experiments

The purpose of this section is to validate the proposed method through numerical experiments compared with analytical and semi-analytical solutions, and also experimental measurements. The main cases considered are a capillary rise of a liquid against a wall with a known analytical solution, and a meniscus rising between two walls with a semi-analytical solution in 2D and 3D. The focus is set on the position of the interface at equilibrium and the corresponding contact angle. Therefore, for these simulations the friction coefficient for the solid is removed for both fluids ($\beta_{\mathrm{SL}} = \beta_{\mathrm{SV}} = 0$). For comparison with some experiments by Pucci et al. [52], the solid is made of cellulose, the liquid is diiodomethane, and the vapour phase is air. The surface energies and surface tension of these phases have been characterised by Pucci et al. [52] and are summarised in Table 1.

Table 1
Input values for the model.

	Solid/vapour – γ_{SV}	Solid/liquid – γ_{SL}	Liquid/vapour – γ_{LV}
Surface tension energy (N/m)	54.7e−3	25.9e−3	50.8e−3

	Vapour	Liquid
Viscosity (Pa s)	1.71e−5	2.76e−3
Density (kg/m^3)	1.292	3.325e3

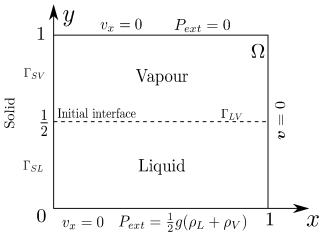

Fig. 4. 2D meniscus against a wall – computational domain and boundary conditions; initially the interface is placed horizontally at $y = \frac{1}{2}$.

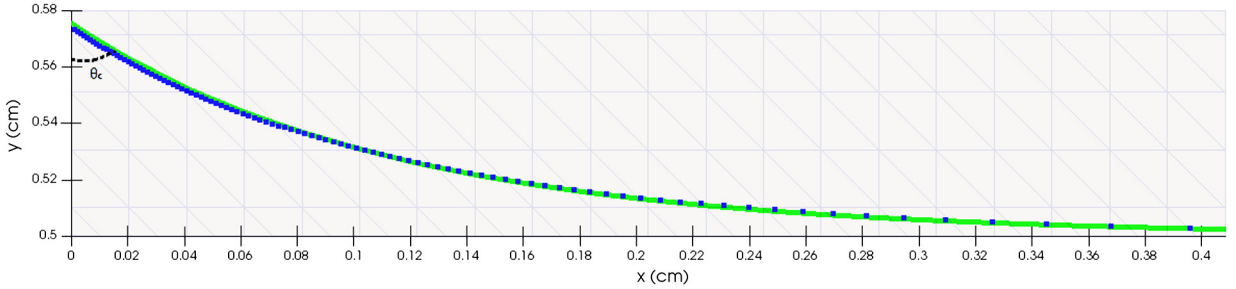

Fig. 5. Meniscus against a wall (left-hand side of the domain), comparison between the Finite Element solution (green curve) and the analytical solution (blue dots).

7.1. Meniscus facing a vertical wall

The first 2D numerical test is a meniscus facing a vertical wall in a unitary domain, as depicted in Fig. 4. Initially, the interface is placed horizontally at $y = \frac{1}{2}$. The fluid can flow in and out of the domain Ω through the top and bottom faces. A Neumann condition is applied on the bottom edge to balance the weight of the two fluids acting along $-\boldsymbol{y}$. The left-hand side of the domain represents the solid boundary with two surface energies (γ_{SV}, γ_{SL}), and the interface between vapour and liquid has one constant surface tension γ_{LV} – see Table 1.

The analytical expression of the static solution is given by de Gennes et al. [5]

$$x - x_0 = \kappa^{-1} \cosh\left(\frac{2\kappa^{-1}}{y}\right) - 2\kappa^{-1}\left(1 - \frac{y^2}{4\kappa^{-2}}\right)^{1/2} \tag{23}$$

where x_0 is the abscissa such that the previous equation (23) yields $y(x = 0) = \sqrt{2}\kappa^{-1}(1 - \sin\theta_c)^{1/2}$, the ordinate of the triple point at equilibrium. The capillary length κ^{-1} is a characteristic of the ratio between capillary and gravitational effects. For the present case, $\kappa^{-1} = \sqrt{\frac{\gamma_{LV}}{\rho_L\, g}} \approx 0.12$ cm and represents the distance over which capillary effects are significant. Therefore, a homogeneous Dirichlet boundary condition can be applied on the right-hand-side edge $(x, y) = (1, y)$ of the domain, as shown in Fig. 4.

For the baseline case of a coarse structured mesh made of 49×49 elements, the simulation is run on a single-core processor and takes 240 s. The mesh contains 2,500 nodes. Two hundred increments are performed with a time step $\Delta t = 2.5\text{e}{-6}$ s, which corresponds to the final time 5e−4 s. At the equilibrium state, the computed profile correlates well with the analytical curve, as shown in Fig. 5. It should be noted that Fig. 5 is a close look on the interface, revealing very low scatters between FE and analytical solutions. As explained in Section 3, the contact angle is a consequence of mechanical equilibrium, which is weakly satisfied at the triple point. From the Young–Laplace equation, the contact angle computed for the chosen data in Table 1 is 55.4°, and our simulation gives a contact angle of 54.7° for a mesh size of 0.02 cm, corresponding to an error of 1.26%.

The convergence of the simulations can be assessed in terms of the error on the meniscus shape as a function of the mesh size. This is reported in Table 2 where the average projection in the x-direction between the computed and theoretical

Table 2
Convergence of the meniscus shape when refining the mesh – mean absolute value $\overline{\Delta_x} = \frac{1}{N}\sum_{i=1}^{N} |x^i_{\text{theo}} - x^i_{\text{num}}|$, with N the number of discretisation points in the interval $x \in [0, 0.4]$.

Mesh size (cm)	$h = 0.02$	$h = 0.01$	$h = 0.005$
$\overline{\Delta_x}$ (cm)	4.1e−3	3.8e−4	7.6e−5

Table 3
Absolute error on the pressure field as a function of the mesh density – $\overline{\Delta_{\text{press}}} = \frac{1}{N_m}\sum_{i=1}^{N_m} |p^{\text{theo}} - p^{\text{comp}}|$, with N_m the number of mesh nodes.

Mesh size (cm)	$h = 0.02$	$h = 0.01$	$h = 0.005$
$\overline{\Delta_{\text{press}}}$ (bar)	4.13e−7	6.12e−8	1.42e−8

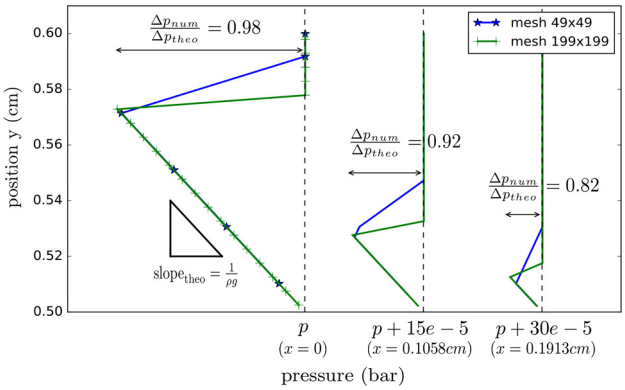

Fig. 6. Meniscus against a wall – pressure profile at three positions x.

menisci is summarised (meshes are structured, as shown in the background of Fig. 5). It can be verified that, with the proposed formulation, meshing with linear elements leads to an abscissa error of the order of a few percents of the mesh size.

Moreover, the pressure field is of major interest, since the jumps in pressure and pressure gradient must be grasped properly in the computations. Fig. 6 represents the position in the y-direction as a function of the pressure profile. In the liquid, the density is higher than in the vapour; this leads to different slopes, lower in the liquid (under Γ_{LV} interface) than in the vapour phase (over Γ_{LV} interface). The pressure field is well characterised by a pressure jump arising from the curvature of the interface, and a gradient pressure jump coming from the change in density. Actually, 98% of the pressure jump is numerically recovered at the triple point on the finest mesh (95% on the coarse mesh), which is the point with the highest curvature. A lower ratio for the two other positions is due to the structured mesh. A local refinement would lead to a better result, but is not mandatory in the simple case. Both pressure and gradient of pressure jumps are correctly described with the enrichment introduced [29] [30]. Overall, the pressure field computed can be also compared with the theoretical pressure field with respect to the mesh size. The data reported in Table 3 permit to verify that this field also is well captured by the method.

Eventually, the velocity field yields some information on the ability of the method to compute a clean (regular) velocity field, even in the neighbourhood of the triple point. The velocity at the first increment is plotted in Fig. 7a. The initial contact angle is equal to 90°. This non-equilibrium state creates a velocity of magnitude 2.2e3 cm/s at the triple point, which brings the system toward the equilibrium state. At the end of the computation, the maximum velocity has a magnitude of 6.3 cm/s, *i.e.* 0.3% of the maximum velocity, which can be considered as representative of the equilibrium state (see Fig. 7b). It can be verified that very few spurious velocities are present, which are inherent to the interface approximation [23] – velocity and pressure spaces are able to capture the physics. But these spurious velocities have no significant effect on the interface development.

In Fig. 8, the position (ordinate) plotted against time for various time steps does not show any significant effect of the choice of the time step. The position at each time step is very close for the four tested time steps. Finally, the change over time in the triple point position is plotted for different time steps in Fig. 8. The curves appear to be superimposed, even for the first time increments – closeup in Fig. 8: the results do not depend on the time step, at least in the considered range. This justifies the staggered Algorithm 1.

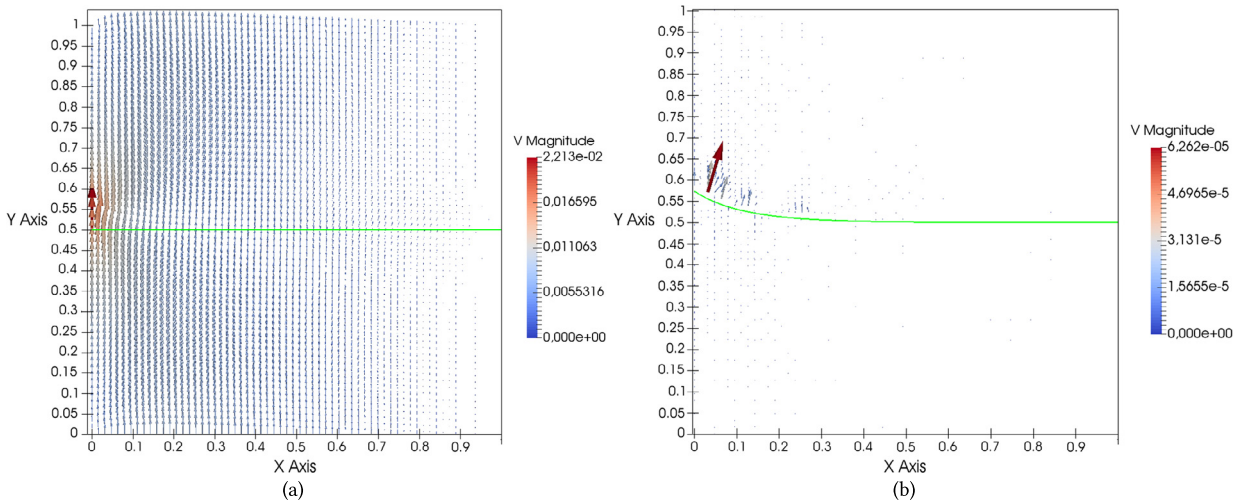

Fig. 7. Meniscus against a wall (left-hand side of the domain), velocity field magnitude in [cm/1e−5 s] at (a) the first and (b) the last increment of the simulation.

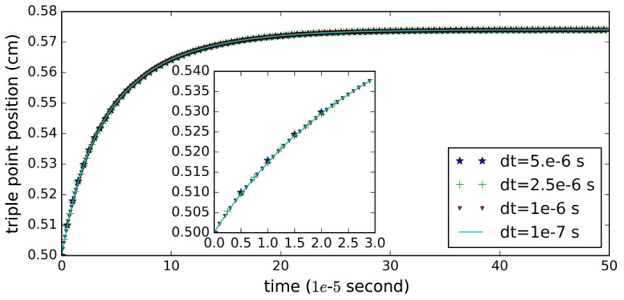

Fig. 8. Ordinate of the triple line during time with four different time steps.

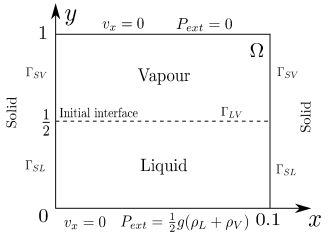

Fig. 9. Computational domain and boundary conditions for a meniscus between two vertical walls.

7.2. Meniscus between two vertical walls

The second case aims at assessing the ability to deal with two menisci, but more importantly at evaluating the interaction between these menisci. This new case is an extension of the first one (same materials considered), with a second vertical wall placed such that the distance between both walls (0.1 cm) is lower than the capillary length (≈0.12 cm), *i.e.* both menisci should interact during the capillary rise. This second wall is placed on the right-hand side of the domain and the rest of the boundary conditions remain unchanged, as presented in Fig. 9. In 2D, the computational cost is still acceptable, the whole domain can be computed without exploiting the inherent symmetry of the problem.

The expected scenario is that one meniscus will form on either side of the domain, then both menisci will interact and merge in order to minimise the global energy. The new merged meniscus increases, since the liquid will be sucked between the walls. When the surface tension force is balanced by the weight of the liquid under the meniscus, the equilibrium position is reached. Unfortunately, no analytical solution is known for this position of the meniscus at equilibrium. However, a semi-analytical solution can be computed, the shape of the meniscus at equilibrium can be derived from the equilibrium of the forces or from a minimisation of the total energy of the system. Both methods are detailed in the following sub-sections for deriving this semi-analytical solution.

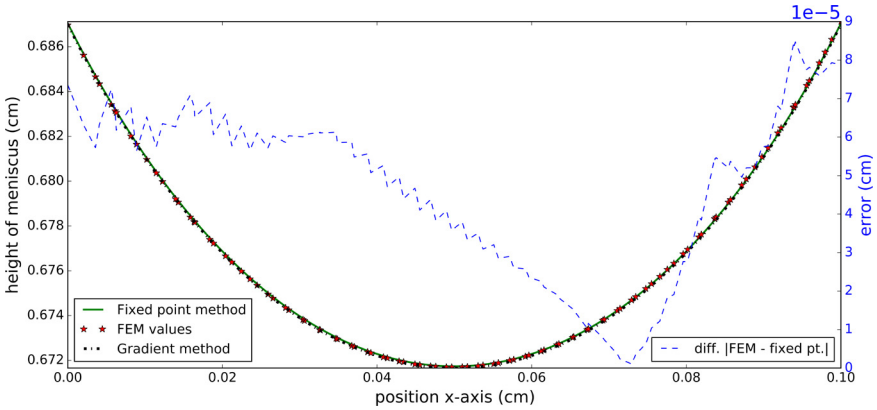

Fig. 10. Comparison of the shape of the meniscus between two vertical walls. The FEM solution is compared with the solutions from the fixed point method and the gradient method.

7.2.1. Validation by the fixed point iterative method – equilibrium of the forces

The meniscus force balance is

$$-\gamma \frac{y''(x)}{\left(1+y'(x)^2\right)^{3/2}} + \rho\, g\, y(x) = 0 \tag{24}$$

with $y(x)$ the height of the meniscus at position x giving the gravity contribution, and $\frac{y''(x)}{\left(1+y'(x)^2\right)^{3/2}}$ the curvature in 2D, which yields the surface-tension force. A fixed point iterative method is used to solve Eq. (24), linearised by considering the length of the interface $\mathrm{d}s = \sqrt{1+y'(x)^2}$ at the previous iteration. The resulting equation is solved using finite differences in one dimension, with the boundary conditions $y'(0) = -1/\tan\theta_c$ and $y'(0.1) = 1/\tan\theta_c$, with $\theta_c = 55.4°$ as the contact angle.

7.2.2. Validation by the gradient method – minimisation of the total energy

The second approach consists in minimising the total energy of the system. The potential energy is equal to $y(x)\,\rho\, g\, \frac{y(x)}{2}\mathrm{d}x$, and the surface tension energy reads $\gamma\,\mathrm{d}s$, with $\mathrm{d}s$ the elementary curvilinear abscissa. Thus the global energy for the system is:

$$E(y, y') = \int_0^1 \left[\frac{1}{2}\rho_L\, g\, y(x)^2 + \gamma\sqrt{1+y'(x)^2}\right]\mathrm{d}x \tag{25}$$

The equilibrium shape of the meniscus will minimise this energy under the boundary conditions already expressed for the first method $y'(0) = -y'(0.1)$. The problem to be solved reads:

$$\min\left\{E(y, y')\,;\ y'(0) = -1/\tan\theta_c \text{ and } y'(0.1) = 1/\tan\theta_c\right\} \tag{26}$$

The minimisation problem is discretised using finite differences and solved using a gradient method as long as the average variation of the unknown is small enough ($< 1e{-}18$).

7.2.3. Results

The FE simulation is carried out using a structured mesh, with a mesh size of 2e−5 m in the x-direction and 5e−5 m in the y-direction, corresponding to 5,000 nodes. 1,000 increments are performed with a time step $\mathrm{d}t = 1e{-}6$ s. As shown in Fig. 10, the FEM solution matches the solution from both fixed point and gradient methods based, respectively, on the force equilibrium and the total energy minimisation. The pointwise absolute error between the FEM solution and the fixed point method is the one represented by the blue dashed curve in Fig. 10, with values between 1e−5 cm and 1e−4 cm, corresponding to a maximum of 0.7% of the meniscus height. The contact angle is also verified, even if weakly prescribed in our formulation, it is equal to 56.6°, versus 54.4° for the semi-analytical solution. The velocity when the system is considered at equilibrium, has a magnitude of 1.4 cm/s, which represents 0.05% of the maximum initial velocity.

7.2.4. Extension to 3D

The test case of a meniscus between two vertical walls is a 2D case. In order to assess the robustness of the method, it can be extended to 3D by extrusion of the domain in the z-direction. The domain considered in the y-direction is reduced, $y \in [0, 0.5]$, and the initial interface is placed at $y = 0.15$. This change aims at reducing the computation cost. 1,000 increments are computed on the unstructured mesh with 32,235 nodes and a time step $\mathrm{d}t = 1e{-}6$ s.

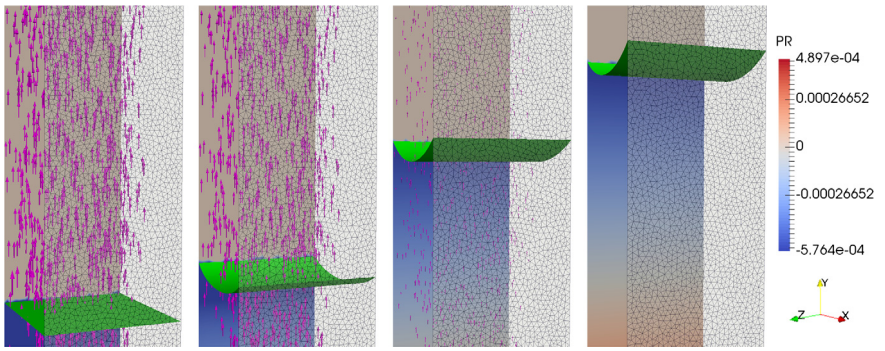

Fig. 11. Finite Element simulation of a meniscus between two walls at four times of the simulation. The first wall (foreground) is represented by its mesh and the second wall (background) is opaque, with pressure contours. The velocity is represented by the magenta arrows ($\|\boldsymbol{v}\|_{\max} = 2.6\mathrm{e}3$ cm/s for (a) and $\|\boldsymbol{v}\|_{\max} = 6.4$ cm/s for (d)) and the liquid–vapour interface is represented by the green surface.

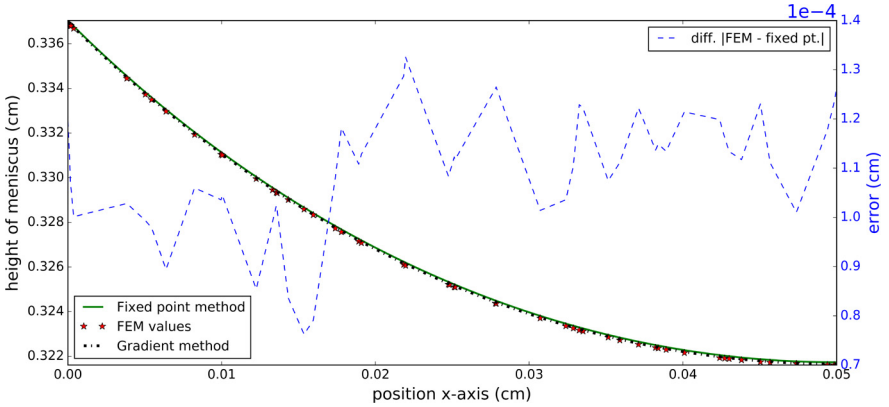

Fig. 12. Comparison of the shape of the meniscus between two vertical walls in three dimensions; one slice in the middle of the domain is analysed. The FE solution is compared with the solution from both fixed point and gradient methods.

Fig. 11a represents the initial position of the meniscus between both vertical walls, with a velocity field that will move the interface. The velocity field is homogeneous, with large magnitudes, since the meniscus is far from its equilibrium position: $\|\boldsymbol{v}\|_{\max} = 2.6\mathrm{e}3$ cm/s. In Fig. 11b–c, the interface is rising, adopting a curved shape, because menisci on each wall interact. Finally, in Fig. 11d, the equilibrium position is considered as being reached with a maximum velocity of 6.4 cm/s, which is negligible compared to the initial maximum velocity.

Following the first 2D analyses, the flow front position can be measured in 3D. Fig. 12 shows a good agreement between the Finite Element solution and the semi-analytical one from the equilibrium of forces and the minimisation of the total energy. In three dimensions, the error is larger than in 2D, due to a coarser mesh: the characteristic mesh size $h_e = 4.0\mathrm{e}{-3}$ cm in 3D, while in 2D, the size of element h_e is equal to $2.0\mathrm{e}{-5}$ and $5.0\mathrm{e}{-5}$ cm in, respectively, the x- and y-directions. The static contact angle is recovered by the numerical simulation with an excess of 3%: it is approximately 57.2° for a targeted theoretical angle of 55.4° computed from the parameters chosen for surface tension and surface energies.

The 3D numerical experiment is intrinsically more challenging, in terms of interface management (element split) for instance, but more especially since the contact point in 2D becomes here a contact line between the three phases with normal/tangent vectors to deal with in space. Still, the method is robust as verified with the position of the meniscus and the contact angle, which are in close agreement with the semi-analytical solutions.

7.3. Cluster of tubes

The last case presented is a 3D simulation of a liquid rising inside a cluster of tubes (Fig. 13). The problem configuration consists in ten vertical parallel glass tubes attached to a fixed horizontal plate, which are placed in contact with a pool of water. The exact position of the tubes is given in Appendix (Fig. 16). The 3D character of this problem is obviously challenging, with a further complexity introduced by the curved solid–fluid interfaces to deal with. The tubes are made of glass, the liquid is water and the vapour is air. The input physical data for the three phases in interaction are reported in Table 4. There does not exist any known solution for such cases, and going towards reality is the aim of robust numerical modelling approaches.

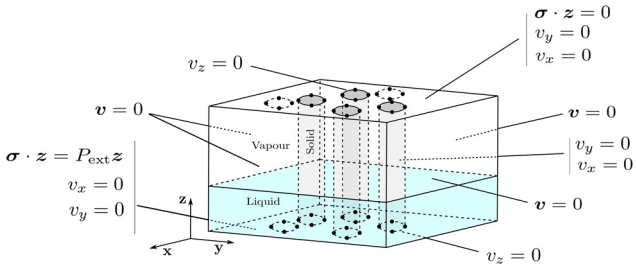

Fig. 13. Cluster of tubes – computational domain and boundary conditions.

Table 4
Input data for the simulation of the cluster of tubes.

	Solid/vapour – γ_{SV}	Solid/liquid – γ_{SL}	Liquid/vapour – γ_{LV}
Surface energy tension (N/m)	60.93e−3	30.03e−3	72.8e−3

	Vapour	Liquid
Viscosity (Pa s)	1.71e−5	1e−3
Density (kg/m^3)	1.292	1e3

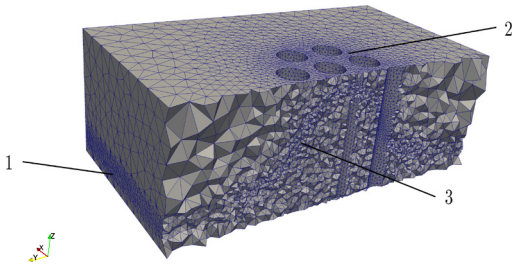

Fig. 14. Mesh for the cluster of tubes.

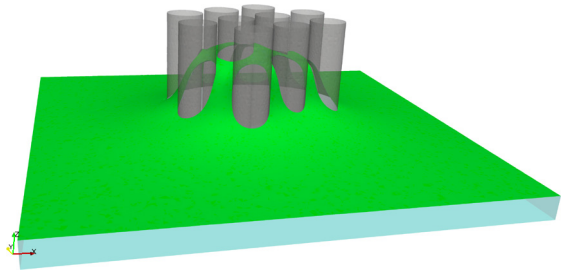

Fig. 15. Equilibrium position of the front of fluid.

As displayed in Fig. 13, boundary conditions are applied on each face of the bounding box of the discretised domain. The capillary length for this case is $\kappa^{-1} \approx 0.27$ cm, which represents less than one third of the distance from any tube to the closest wall. Consequently, on the four lateral faces of the domain, the velocity is prescribed as homogeneous Dirichlet conditions, *i.e.* $\boldsymbol{v} = \boldsymbol{0}$, since the tubes are far enough from these boundaries. The velocity at the top and bottom of each tube is prescribed as null in the z-direction. This choice aims at removing the tangent term from equation (13) and has no influence on the steady state solution, since the velocity vanishes at equilibrium. Finally, a fluid pressure corresponding to hydrostatic pressure is prescribed at the contact with water (bottom face), and a zero pressure is prescribed on the top face.

The mesh, presented in Fig. 14, is refined in three regions (denoted 1, 2, 3 in the figure), in order to put the unknowns in strategic locations. The first region corresponds to the interface location outside the cluster. The second one is the intra-cluster region. This refinement aims to describe with a greater precision the front of fluid in regions with a high degree of curvature. Finally, the third region corresponds to the expected equilibrium position. This position has been inferred from a first computation using a coarser mesh. Hundred increments are performed with a time step of $\mathrm{d}t = 5\text{e}{-6}$ s on the mesh from Fig. 14 containing 91,701 nodes.

The equilibrium position of the meniscus is shown in Fig. 15. The transparent grey tubes in the center represent the glass tubes, and the interface between the air and water is the green surface. The liquid underneath is coloured in light

blue. The maximal velocity at the beginning is at the triple line with a value of 3.3e−2 cm/s, when at the end the maximal value is 5.7e−3 cm/s. One can verify that the fluid has risen between the tubes separated by a distance smaller than the capillary length. On the edge of the cluster, a standard meniscus is formed with the pool of water and vanishes on the domain edges.

8. Conclusion

An original numerical method has been proposed in this paper to simulate capillary effects within the framework of continuum mechanics for two-fluid flows. This method relies on several key features. Following our previous studies on infusion process simulation [14] [15], the Stokes system is solved in velocity/pressure by using a FE-P1/P1 approximation, stabilised with an ASGS method. A *level-set* technique is used to capture the liquid–vapour interface evolution. The transport equation is solved by a SUPG-FE method, with a linear approximation of the *level-set* function and a Hamilton–Jacobi formulation for the redistanciation step. Concerning the specific tension-surface-driven problem, pressure enrichment at the interface permits to capture both pressure and gradient pressure jumps [29] [30]. An original formulation of the mechanical problem at liquid/vapour, liquid/solid, and vapour/solid interfaces leads to a weakening and a natural prescription of the mechanical equilibrium at the contact line [21]. As for the time discretisation, a semi-implicit treatment on the surface tension term [44] yields a stabilisation that removes to a large extent the time step dependency.

Various numerical tests have permitted to verify the robustness of the method, first in 2D for a simple meniscus with analytical solution and also for combining menisci with semi-analytical solutions. Then in 3D a rising meniscus was successfully represented, and eventually a capillary rising in a cluster of tubes was considered. The contact angle was properly recovered, thanks to the contact line mechanical equilibrium weakly imposed into the formulation. The discontinuities across the interface were correctly described, avoiding any spurious velocities. The robustness of the method has been successfully tested against a challenging 3D case with multiple curved interfaces.

The proposed method requires only one mesh for both fluid and *level-set* problems, with no further refinement to capture discontinuities. Each problem has its own formulation and stabilisation, and is solved successively in the staggered approach using a time step which is not restrained by the discretisation. Further work will focus on the application of this method to void formation in LRI processes and to the dynamic stage of wicking, provided sufficient experimental data are made available.

Appendix A

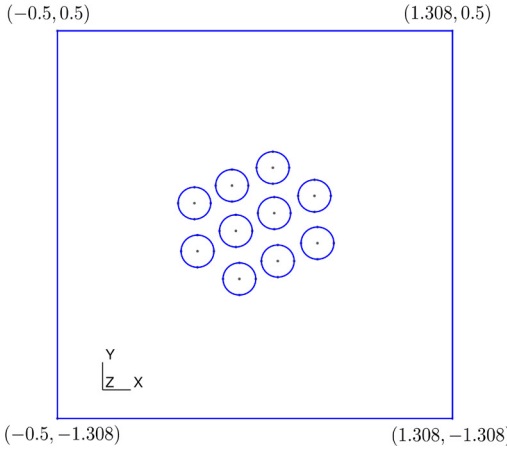

$center1 = (0.48602745, -0.13835841)$ $radius1 = 0.0746808364151$
$center2 = (0.29900382, -0.221544)$ $radius2 = 0.0746703038164$
$center3 = (0.67654356, -0.2695707)$ $radius3 = 0.0748519216834$
$center4 = (0.12705528, -0.30379272)$ $radius4 = 0.0745648960019$
$center5 = (0.49247028, -0.35015427)$ $radius5 = 0.0748109854366$
$center6 = (0.31678395, -0.43307568)$ $radius6 = 0.074972939889$
$center7 = (0.6901677, -0.49001514)$ $radius7 = 0.0750275826836$
$center8 = (0.14113587, -0.52767507)$ $radius8 = 0.0750910067152$
$center9 = (0.50869236, -0.5736276)$ $radius9 = 0.074939251258$
$center10 = (0.33286374, -0.6569106)$ $radius10 = 0.0749110737251$

Fig. 16. Position of the tubes.

References

[1] R. Masoodi, K.M. Pillai, Wicking in Porous Materials, Taylor & Francis, 2013.
[2] D. Pino Muñoz, J. Bruchon, S. Drapier, F. Valdivieso, A finite element-based level set method for fluid-elastic solid interaction with surface tension, Int. J. Numer. Methods Biomed. Eng. 93 (9) (2013) 919–941.
[3] J. Bruchon, S. Drapier, F. Valdivieso, 3d finite element simulation of the matter flow by surface diffusion using a level set method, Int. J. Numer. Methods Biomed. Eng. 86 (7) (2011) 845–861.
[4] D. Seveno, A. Vaillant, R. Rioboo, H. Adão, J. Conti, J. De Coninck, Dynamics of wetting revisited, Langmuir 25 (22) (2009) 13034–13044.
[5] P.-G. De Gennes, F. Brochard-Wyart, D. Quéré, Capillarity and Wetting Phenomena – Drops, Bubbles, Pearls, Waves, 2002.
[6] A. Marchand, S. Das, J.H. Snoeijer, B. Andreotti, Contact angles on a soft solid: from Young's law to Neumann's law, Phys. Rev. Lett. 109 (23) (2012).
[7] T.D. Blake, The physics of moving wetting lines, J. Colloid Interface Sci. 299 (1) (2006) 1–13.

[8] M.V. Bruschke, S.G. Advani, A finite element/control volume approach to mold filling in anisotropic porous media, Polym. Compos. 11 (6) (1990) 398–405.
[9] F. Trochu, E. Ruiz, V. Achim, S. Soukane, Advanced numerical simulation of liquid composite molding for process analysis and optimization, Composites, Part A, Appl. Sci. Manuf. 37 (6) (2006) 890–902.
[10] H. Hu, R.G. Larson, Analysis of the microfluid flow in an evaporating sessile droplet, Langmuir 21 (9) (2005) 3963–3971.
[11] H. Combeau, M. Bellet, Y. Fautrelle, D. Gobin, E. Arquis, O. Budenkova, B. Dussoubs, Y. du Terrail, A. Kumar, C.-A. Gandin, B. Goyeau, S. Mosbah, T. Quatravaux, M.A. Rady, M. Založnik, Analysis of a numerical benchmark for columnar solidification of binary alloys, IOP Conf. Ser., Mater. Sci. Eng. 33 (2012) 12–27.
[12] P. Celle, S. Drapier, J.-M. Bergheau, Numerical modelling of liquid infusion into fibrous media undergoing compaction, Eur. J. Mech. A, Solids 27 (4) (2008) 647–661.
[13] G. Pacquaut, J. Bruchon, N. Moulin, S. Drapier, Combining a level-set method and a mixed stabilized P1/P1 formulation for coupling Stokes–Darcy flows, Int. J. Numer. Methods Fluids 69 (2) (2012) 459–480.
[14] L. Abouorm, R. Troian, S. Drapier, J. Bruchon, N. Moulin, Stokes–Darcy coupling in severe regimes using multiscale stabilisation for mixed finite elements: monolithic approach versus decoupled approach, Eur. J. Comput. Mech. 23 (3–4) (2014) 113–137.
[15] M. Blais, N. Moulin, P.-J. Liotier, S. Drapier, Resin infusion-based processes simulation: coupled Stokes–Darcy flows in orthotropic preforms undergoing finite strain, Int. J. Mater. Form. 10 (1) (2015) 43–54.
[16] M.F. Pucci, P.-J. Liotier, S. Drapier, Capillary wicking in a fibrous reinforcement – orthotropic issues to determine the capillary pressure components, Composites, Part A, Appl. Sci. Manuf. 77 (2015) 133–141.
[17] C. Hae Park, A. Lebel, A. Saouab, J. Bréard, W.I. Lee, Modeling and simulation of voids and saturation in liquid composite molding processes, Composites, Part A, Appl. Sci. Manuf. 42 (6) (2011) 658–668.
[18] E. Lopez, A. Leygue, E. Abisset-Chavanne, S. Comas-Cardona, C. Aufrere, C. Binetruy, F. Chinesta, Flow modeling of linear and nonlinear fluids in two and three scale fibrous fabrics, Int. J. Mater. Form. 10 (3) (2015) 317–328.
[19] S. Osher, J.A. Sethian, Fronts propagating with curvature-dependent speed: algorithms based on Hamilton–Jacobi formulations, J. Comput. Phys. 79 (1) (1988) 12–49.
[20] L. Benazzouk, E. Arquis, N. Bertrand, C. Descamps, M. Valat, Motion of a liquid bridge in a capillary slot: a numerical investigation of wettability and geometrical effects, Houille Blanche 3 (2013) 50–56.
[21] J. Bruchon, N. Moulin, Y. Liu, New variational formulation of the triple junction equilibrium with applications to wetting problems, in: Methods in Applied Sciences and Engineering, ECCOMAS Congress 2016, Crete Island, Greece, 2016.
[22] S.F. Kistler, P.M. Schweizer, Liquid Film Coating: Scientific Principles and Their Technological Implications, Chapman & Hall, 1997.
[23] S. Ganesan, G. Matthies, L. Tobiska, On spurious velocities in incompressible flow problems with interfaces, Comput. Methods Appl. Mech. Eng. 196 (7) (2007) 1193–1202.
[24] B. Lafaurie, C. Nardone, R. Scardovelli, S. Zaleski, G. Zanetti, Modelling merging and fragmentation in multiphase flows with SURFER, J. Comput. Phys. 113 (1) (1994) 134–147.
[25] M.M. Francois, S.J. Cummins, E.D. Dendy, D.B. Kothe, J.M. Sicilian, M.W. Williams, A balanced-force algorithm for continuous and sharp interfacial surface tension models within a volume tracking framework, J. Comput. Phys. 213 (1) (2006) 141–173.
[26] M. Discacciati, D. Hacker, A. Quarteroni, S. Quinodoz, S. Tissot, F.M. Wurm, Numerical simulation of orbitally shaken viscous fluids with free surface, Int. J. Numer. Methods Fluids 71 (3) (2013) 294–315.
[27] J. Chessa, T. Belytschko, An extended finite element method for two-phase fluids, J. Appl. Mech. 70 (1) (2003) 10–17.
[28] P.D. Minev, T. Chen, K. Nandakumar, A finite element technique for multifluid incompressible flow using Eulerian grids, J. Comput. Phys. 187 (1) (2003) 255–273.
[29] R.F. Ausas, G.C. Buscaglia, S.R. Idelsohn, A new enrichment space for the treatment of discontinuous pressures in multi-fluid flows, Int. J. Numer. Methods Fluids 70 (7) (2012) 829–850.
[30] H. Coppola Owen, R. Codina, Improving Eulerian two-phase flow finite element approximation with discontinuous gradient pressure shape functions, Int. J. Numer. Methods Fluids 49 (12) (2005) 1287–1304.
[31] J.E. Sprittles, Y.D. Shikhmurzaev, Finite element simulation of dynamic wetting flows as an interface formation process, J. Comput. Phys. 233 (1) (2013) 34–65.
[32] R.A. Sauer, A contact theory for surface tension driven systems, Math. Mech. Solids 21 (3) (2014) 305–325.
[33] A. Reusken, X. Xu, L. Zhang, Finite element methods for a class of continuum models for immiscible flows with moving contact lines, Int. J. Numer. Methods Fluids 84 (5) (2017) 268–291.
[34] G.C. Buscaglia, R.F. Ausas, Variational formulations for surface tension, capillarity and wetting, Comput. Methods Appl. Mech. Eng. 200 (45–46) (2011) 3011–3025.
[35] R.W. Style, R. Boltyanskiy, Y. Che, J.S. Wettlaufer, L.A. Wilen, E.R. Dufresne, Universal deformation of soft substrates near a contact line and the direct measurement of solid surface stresses, Phys. Rev. Lett. 110 (6) (2013).
[36] T.J.R. Hughes, Multiscale phenomena: Green's functions, the Dirichlet-to-Neumann formulation, subgrid scale models, bubbles and the origins of stabilized methods, Comput. Methods Appl. Mech. Eng. 127 (1–4) (1995) 387–401.
[37] T.J.R. Hughes, G.R. Feijoo, L. Mazzei, J.B. Quincy, The variational multiscale method – a paradigm for computational mechanics, Comput. Methods Appl. Mech. Eng. 166 (1–2) (1998) 3–24.
[38] R. Codina, A stabilized finite element method for generalized stationary incompressible flows, Comput. Methods Appl. Mech. Eng. 190 (20–21) (2001) 2681–2706.
[39] E. Hachem, B. Rivaux, T. Kloczko, H. Digonnet, T. Coupez, Stabilized finite element method for incompressible flows with high Reynolds number, J. Comput. Phys. 229 (23) (2010) 8643–8665.
[40] L. Abouorm, N. Moulin, J. Bruchon, S. Drapier, Monolithic approach of Stokes–Darcy coupling for LCM process modelling, in: 16th ESAFORM Conference on Material Forming, ESAFORM 2013, Key Eng. Mater. 554–557 (2013) 447–455.
[41] Y. Liu, N. Moulin, J. Bruchon, P.-J. Liotier, S. Drapier, Towards void formation and permeability predictions in LCM processes: a computational bifluid–solid mechanics framework dealing with capillarity and wetting issues, C. R. Mecanique 344 (4–5) (2016) 236–250.
[42] H. Sauerland, T.P. Fries, The stable XFEM for two-phase flows, Comput. Fluids 87 (2013) 41–49.
[43] S. Groß, V. Reichelt, A. Reusken, A finite element based level set method for two-phase incompressible flows, Comput. Vis. Sci. 9 (4) (2006) 239–257.
[44] E. Bänsch, Finite element discretization of the Navier–Stokes equations with a free capillary surface, Numer. Math. 88 (2) (2001) 203–235.
[45] G. Dziuk, An algorithm for evolutionary surfaces, Numer. Math. 58 (1) (1990) 603–611.
[46] G. Dziuk, C.M. Elliott, Finite elements on evolving surfaces, IMA J. Numer. Anal. 27 (2) (2007) 262–292.
[47] S. Groß, A. Reusken, Finite element discretization error analysis of a surface tension force in two-phase incompressible flows, SIAM J. Numer. Anal. 45 (4) (2007) 1679–1700.
[48] A.N. Brooks, T.J.R. Hughes, Streamline upwind/Petrov–Galerkin formulations for convection dominated flows with particular emphasis on the incompressible Navier–Stokes equations, Comput. Methods Appl. Mech. Eng. 32 (1–3) (1982) 199–259.

[49] J. Crank, P. Nicolson, A practical method for numerical evaluation of solutions of partial differential equations of the heat-conduction type, Math. Proc. Camb. Philos. Soc. 43 (01) (1947) 50–67.
[50] M. Sussman, P. Smereka, S. Osher, A level set approach for computing solutions to incompressible two-phase flow, J. Comput. Phys. 114 (1) (1994) 146–159.
[51] D. Peng, B. Merriman, S. Osher, H. Zhao, M. Kang, A PDE-based fast local level set method, J. Comput. Phys. 155 (2) (1999) 410–438.
[52] M.F. Pucci, P.-J. Liotier, S. Drapier, Tensiometric method to reliably assess wetting properties of single fibers with resins: validation on cellulosic reinforcements for composites, Colloids Surf. A, Physicochem. Eng. Asp. 512 (2017) 26–33.